Breaking dynamic inversion symmetry in a racemic mixture using simple trains of laser pulses

Thomas, Esben Folger; Henriksen, Niels Engholm

Published in:
Journal of Chemical Physics

Link to article, DOI:
10.1063/1.5063536

Publication date:
2019

Document Version
Peer reviewed version

This manuscript was accepted by J. Chem. Phys. Click here to see the version of record.

Breaking Dynamic Inversion Symmetry in a Racemic Mixture Using Simple Trains of Laser Pulses

Esben F. Thomas and Niels E. Henriksen

Department of Chemistry, Technical University of Denmark, Building 206, DK-2800 Kongens Lyngby, Denmark

Recent advances in ultrafast laser technology hint at the possibility of using shaped pulses to generate deracemization via selective enantiomeric conversion; however, experimental implementation remains a challenge and has not yet been achieved. Here, we describe an experiment that can be considered an accessible intermediate step on the road towards achieving laser induced deracemization in a laboratory. Our approach consists of driving a racemic mixture of 3D oriented 3,5-difluoro-3′,5′-dibromobiphenyl ($F_2H_3C_6 - C_6H_3Br_2$) molecules with a simple train of Gaussian pulses with alternating polarization axes. We use arguments related to the geometry of the field/molecule interaction to illustrate why this will increase the amplitude of the torsional oscillations between the phenyl rings while simultaneously breaking the inversion symmetry of the dynamics between the left- and right-handed enantiomeric forms, two crucial requirements for achieving deracemization. We verify our approach using numerical simulations, and show that it leads to significant and experimentally measurable differences in the internal enantiomeric structures when detected by Coulomb explosion imaging.

I. INTRODUCTION

Deracemization occurs when a racemic mixture of molecules is transformed into a mixture containing an excess of a single enantiomer. The majority of the work done on deracemization at present time has been concerned with the use of chemical reagents to separate or transform enantiomers (see, e.g., refs 1 and 2).

A number of theoretical studies have also demonstrated the feasibility of a fundamentally different approach, where deracemization is achieved using coherent laser light (see, e.g., refs 3–13). Many of these theoretical investigations have been based around determining the shape of the deracemizing laser pulse using some kind of optimization algorithm; for example in a previous study[14] done by our group we demonstrated theoretically that a genetic algorithm[15] can be used to optimize the spectral phase components[16] of two nonresonant, linearly polarized Gaussian laser pulses with polarization axes rotated 13° away from each other in a way that leads to selective enantiomeric conversion of a racemic mixture of 3D-oriented, 3,5-difluoro-3′,5′-dibromobiphenyl ($F_2H_3C_6 - C_6H_3Br_2$) molecules. However, achieving laser-induced deracemization in a laboratory has not yet been achieved. This is partly because experimentalists still consider it a "high risk" venture; the difficulty of performing the experiment means that it will require the allocation of significant resources.

Here, we therefore propose a more modest experiment that can be considered an intermediate step on the road towards fully achieving laser induced deracemization. Using an experimental setup similar to the one described in ref. 14, we theoretically demonstrate that applying a relatively simple series of driving laser pulses to a gas phase racemic mixture of 3D aligned/oriented $F_2H_3C_6 - C_6H_3Br_2$ molecules can lead to significant and measurable differences in the internal dynamics and structure between the left- and right-handed enantiomeric forms, effectively transforming a racemic 50/50 mixture into a 26/74 mixture that is skewed towards one of the enantiomeric species. The key difference between this work and that performed in ref. 14 is that the results presented here do not require significant optimization of the laser pulse shape; instead we exploit some of the general principles that we uncovered by analyzing the optimized fields in ref. 14 to "manually" construct the pulse train in a way designed to make experimental implementation more feasible.

This manuscript was accepted by J. Chem. Phys. Click here to see the version of record.

II. BACKGROUND INFORMATION

The experimental and theoretical details pertaining to $F_2H_3C_6 - C_6H_3Br_2$ and similar molecular systems are covered in refs. 14, 17–19. To summarize, $F_2H_3C_6 - C_6H_3Br_2$ has an axially chiral structure where torsional rotation around the stereogenic axis leads to transformations between left- and right-handed enantiomeric forms. Gas-phase $F_2H_3C_6 - C_6H_3Br_2$ molecules can be oriented in 3D using an elliptical alignment pulse combined with a static electric field[20], where the alignment pulse is defined in lab frame coordinates $(\hat{x}, \hat{y}, \hat{z})$ as $\mathbf{E}_0(t) = E_{0z}\hat{z} + E_{0x}\hat{x}$, where the minor (major) polarization axis of the elliptical pulse lies along the $\hat{x}$ ($\hat{z}$) lab frame axis. It has been demonstrated experimentally[19] that the most polarizable axis (MPA) of the molecules will align along $\hat{z}$ with the major alignment pulse axis, and the second most polarizable axis (SMPA) of the molecules will align with the minor alignment axis along $\hat{x}$, as shown in figure 1.

As in our previous work in ref. 14, all laser pulses described in this paper couple to the molecular polarizability functions by way of the dynamic Stark effect[21–23], which is proportional to the square of the field envelope times the molecular polarizability term. An advantage of this method is therefore that we are not limited by the carrier frequency of the laser, as it can be shown that the molecules will only respond to changes in the electric field envelope in the dynamic Stark regime. A detailed description of the polarizability surfaces used in our model can be found in section Is of the supporting information in ref. 14 (note that there is a minor error here; the form of the $\alpha_{xx,yy}(\phi_d)$ should be given by $A_{xx,yy}\cos(2\phi_d) + B_{xx,yy}$ and $\alpha_{xy}(\phi_d)$ is given by $A_{xy}\sin(2\phi_d) + B_{xy}$).

As outlined in refs. 14 and 19, if we treat the F and Br substituted rings as two fixed rotors rotating in the $\hat{x}\hat{y}$ plane, we can represent the system in 2 dimensions using ϕ_{F} and ϕ_{Br} as coordinates describing, respectively, the angle of the F and Br substituted ring in relation to the $\hat{x}$ axis. The internal potential energy of the molecule is a function of the relative dihedral angle $\phi_d = \phi_{\mathrm{Br}} - \phi_{\mathrm{F}}$. The explicit form of the potential function we use in our model, which was calculated as a minimum energy path, can be found in section IIs of the supporting information in ref. 14. The nonresonance and relatively large (ns) temporal width of the adiabatic alignment pulse means we can model its effects on the system by adding a time-independent perturbation to the field-free potential. This creates local minima in the 2D potential surface that correspond to rotational alignment of the rings

in the $\hat{x}\hat{y}$ plane, as shown, e.g., in figure 1 of ref. 14. After using the relaxation method[24] to calculate the first few eigenstates of the system, the initial conditions of the simulation are chosen as an incoherent sum of densities associated with localized superpositions confined to a single potential well, as described in ref. 14.

As also shown in refs. 14 and 17, this 2D representation can be transformed into a coordinate system that decouples the kinetic energy of the "external" motion (i.e. changes in the weighted rotational angle Φ) of the molecules from their "internal" dynamics (i.e. changes in the relative dihedral angle ϕ_d). Details of how the weighted rotational angle Φ is constructed, and the corresponding decoupled Hamiltonian, can be found on page 3 of ref. 17.

In the work performed in ref. 17 it is demonstrated that cooling a gas-phase population of $F_2H_3C_6 - C_6H_3Br_2$ molecules to a few Kelvin will hinder the internal rotation, and the dihedral angle ϕ_d between the ring planes will become fixed at 39° and −39°. As figure 2 demonstrates, these angular configurations correspond to two different stable structures that are each other's mirror image, that is, an enantiomeric pair. Here we adopt the notation of labelling the 39° and −39° configurations as S_a and R_a enantiomers, respectively.

In a general sense, the deracemization process is characterized by selective changes in the internal structure of one of the enantiomers. For this reason, the process can be purely quantified by only following the internal dynamics of the R_a and S_a nuclear wave packets in the ϕ_d coordinate. However, as we shall soon demonstrate, the relative angle between the molecular orientations in Φ and the polarization axis of the driving pulse is also a critical factor to take into account for deracemization to be possible. We now introduce a concept that will be important in the following analyses; namely the structural symmetry axis of the system. Assuming that the dihedral angles of the enantiomers have equal and opposite signs, the structural symmetry axis is defined as the "mirror line" in the $\hat{x}\hat{y}$ plane that will perfectly reflect the structure and orientation of the R_a (S_a) enantiomer into its mirrored S_a (R_a) counterpart. Mathematically, this axis lies in the $\hat{x}\hat{y}$ plane where its angle in relation to the the $\hat{x}$ axis is defined by the mean value of the weighted rotational angles of both enantiomers, i.e.

$$\hat{\theta}_{\text{sym}} = \cos\left(\frac{\Phi_{R_a} + \Phi_{S_a}}{2}\right)\hat{x} - \sin\left(\frac{\Phi_{R_a} + \Phi_{S_a}}{2}\right)\hat{y} \tag{1}$$

For example, the structural symmetry axis of the enantiomers will lie along the $\hat{x}$ axis when

This manuscript was accepted by J. Chem. Phys. Click here to see the version of record.

FIG. 1. Molecular structure of 3, 5-Difluoro-3′, 5′-dibromobiphenyl ($F_2H_3C_6-C_6H_3Br_2$). The most polarizable axis (MPA) and second most polarizable axis (SMPA) are represented by respective red and blue dotted lines in the $\hat{x}\hat{z}$ plane. Note that the stereogenic axis of the molecule is identical to the MPA. In the simulations performed throughout this article, the MPA is always oriented along the lab frame $\hat{z}$ axis with the Br-substituted ring pointing in the positive direction as shown. The elliptical orientation pulse $\mathbf{E}_0$ propagates along the $\hat{y}$ axis (see, e.g., figure 5), and the vertical (horizontal) pink arrows show the direction of its major (minor) polarization axes, denoted by $\mathbf{E}_{0z}$ ($\mathbf{E}_{0x}$).

FIG. 2. Top-down view along the $\hat{z}$ axis of the 3D-oriented R_a and S_a enantiomers when their SMPA's (dotted blue lines) are aligned with the minor polarization axis of the alignment pulse $\mathbf{E}_{0x}$ (pink arrows). From this view, the stereogenic axes are orthogonal to the page and located in the center of each molecule (i.e. where the thick black arrows start). The dihedral angle (dashed black arcs) in this coordinate system is defined as $\phi_d = \phi_{\mathrm{Br}} - \phi_{\mathrm{F}}$, where ϕ_{Br} and ϕ_{F} are the respective rotational angles of the Br- and F- substituted rings around the stereogenic $\hat{z}$ axis with respect to $\hat{x}$. In this configuration, the weighted rotational angles Φ (black arrows) of the enantiomers have equal and opposite signs, i.e. the structural symmetry axis of the system $\hat{\theta}_{\mathrm{sym}}$ is aligned with the lab frame $\hat{x}$ axis (see equation 1). Note that the angular coordinate system used here and throughout the rest of this article is defined such that the positive direction corresponds to clockwise rotations.

they are in their initial 3D aligned state, as can be seen in figure 2.

In ref. 14 it was discovered that the shaped pulses are able to achieve deracemization by concurrently satisfying at least two conditions; the dihedral oscillations in ϕ_d must become large enough for at least one of the enantiomeric wave packets to be able to move over the potential barrier separating the enantiomeric species, and the inversion symmetry of the dynamics in ϕ_d between the two enantiomers must be broken, i.e. the dynamics of the torsional oscillations in the R_a and S_a enantiomer must evolve in a way that leads to them becoming dissimilar.

FIG. 3. As discussed in the article text, when the molecules are in their initial 3D oriented state, the application of a kick pulse polarized in the $\hat{x}\hat{y}$ plane will exert a force on the molecular wave packets. Panels (1a), (2a), and (3a) show the field perturbed potential energy surfaces in the (Φ, ϕ_d) coordinate system when the polarization axis of the applied field is respectively rotated 0°, 15° and 30° away from the alignment field axis. The solid and dotted arrows show the ϕ_d and Φ components of the respective initial wave packet acceleration vectors of the R_a (red) and S_a (blue) enantiomers. Panels (1b), (2b), and (3b) show corresponding sketches of the molecular orientations in space and the changing polarization direction of the applied field. Here, the solid curved arrows illustrate the "pinching" forces that the field will apply to the torsional motion, and the dotted arrows show the direction and magnitude of the field induced rotation in the Φ coordinate.

III. SYMMETRY BREAKING PRINCIPLES

At this point, it is instructive to look at how the potential energy surfaces of the initial 3D-oriented enantiomers are modified in the presence of a nonadiabatically applied 10 TW/cm^2 field when the polarization axis of the field is rotated away from the $\hat{x}$ axis in the $\hat{x}\hat{y}$ plane by various angles. Panels (1a), (2a) and (3a) in figure 3 show the potential energy surfaces when the polarization axis of the applied field is respectively rotated 0°, 15°, and 30° away from the $\hat{x}$ axis, where the blue (red) dots show the initial S_a (R_a) wave packet expectation positions. Switching on the 10 TW/cm^2 field creates a potential gradient that causes the wave packets to accelerate. The solid blue (red) arrows in the same panels indicate the magnitude and direction of the initial S_a (R_a) wave packet acceleration vectors when projected onto the ϕ_d coordinate, and the blue (red) dotted lines show the equivalent acceleration in the Φ coordinate. Panels (1b), (2b), and (3b) in figure 3 show a sketch of the field polarization axes in relation to the oriented molecules in lab-frame coordinates, as well as illustrating how the acceleration vectors depicted in panels (1a), (2a), and (3a) are represented in the "real" molecular geometry.

Panels (1a) and (1b) in figure 3 show that there will be no initial movement in the Φ coordinate when the polarization axis of the applied field is aligned with the $\hat{x}$ axis. Additionally, the ϕ_d component of the R_a and S_a acceleration vectors will have equal lengths and point in opposite directions. Panel (1b) illustrates that this corresponds to applying

This manuscript was accepted by J. Chem. Phys. Click here to see the version of record.

identical "pinching" forces to the rings of both enantiomers. The fact that the force vectors felt by each enantiomer are mirrored copies of each other can be understood geometrically by noting that the polarization axis of the driving field is parallel to the structural symmetry axis $\hat{\theta}_{\text{sym}}$ shared by the enantiomers; in a sense the field is "seeing" two identical mirrored versions of the exact same molecule from this angle, so the dynamic response of the enantiomers to the field will necessarily also be mirrored across the $\hat{\theta}_{\text{sym}}/\hat{x}$ axis at all subsequent times as long as the driving field remains polarized in this direction.

In a classical sense, evolving the system dynamics in time on the field-perturbed potential energy surface shown in panel (1a) of figure 3 will lead to torsional vibrations in ϕ_d as the wave packets oscillate in the potential wells created by the external field. Furthermore, applying the $\hat{x}$-aligned field dynamically using, e.g., a train of pulses with spacings approximately equal to the torsional vibrational period will result in resonant driving that increases the amplitude of this torsional motion, a phenomenon that is well understood[23,25] and has been demonstrated experimentally on similar molecules[19]. This satisfies the first criteria that must be met for deracemization to occur; namely that the amplitude of the torsional vibrations must become large enough to facilitate wave packet transfer over the saddle point located at $\phi_d = 0$ that separates the enantiomeric forms. Note, however, that the structure of the R_a and S_a enantiomers will remain symmetrical across the polarization axis of the driving field as we propagate the dynamics forward in time, i.e. the molecules will remain mirror images of each other as long as the driving field is polarized along $\hat{\theta}_{\text{sym}}/\hat{x}$. This means that any transformation that takes place in one enantiomer will always take place in its mirrored counterpart as well, effectively making deracemization impossible.

Breaking the dynamic inversion symmetry while simultaneously increasing the amplitude of the torsional vibrations requires a slightly different approach. As stated, the center and right columns in figure 3 show what happens when the polarization axis of the driving field is de-aligned from the structural symmetry axis by, respectively, 15° and 30° in the $\hat{x}\hat{y}$ plane. There are a number of things to note here. First of all, both enantiomer wave packets will start to accelerate in the positive direction of the Φ coordinate as the molecules rotate around the $\hat{z}$ axis towards the polarization axis of the driving field. Secondly, the magnitude of the acceleration vectors in ϕ_d generally become smaller and, most importantly, *dissimilar* as the de-alignment angle is increased.

These differences in the accelerations that the R_a and S_a torsional wave packets will

FIG. 4. The four panels illustrate how the amplitude of the dihedral oscillations can be driven while maintaining the asymmetrical nature of the enantiomer/field interaction by continually alternating the polarization axes of the driving pulses (see article text for full explanation). The dashed black lines represent the angle structural symmetry axis shared by the enantiomers $\hat{\theta}_{\text{sym}}$.

FIG. 5. A sketch of the initial 3D oriented R_a/S_a system, and two pulse trains with field polarization axes rotated $\pm 8.5^\circ$ away from the $\hat{x}$ axis in the $\hat{x}\hat{y}$ plane. As sketched in figure 4, driving the molecules with these pulse trains will increase the torsional oscillations and simultaneously break the dynamic inversion symmetry of the torsional motion between the enantiomers (see figure 6 for the simulated results). For reference the alignment pulse is also shown in pink.

experience as the polarization axis of the driving field is rotated away from the structural symmetry axis of the enantiomers can be understood if we once again consider the geometry of the overall field/molecular configuration. Unlike the previously discussed case where the polarization axis was aligned with the $\hat{\theta}_{\text{sym}}/\hat{x}$ axis, the field is now effectively "seeing" the R_a and S_a molecules from two different angles. For example, in panel (3b) of figure 3 it can be seen that the polarization axis of the 30° rotated field is now nearly parallel with the F-ring of the R_a enantiomer, and rotated roughly 60° away from the F-ring of the S_a enantiomer. These geometrical differences lead to subtle changes in the way the field interacts with each enantiomer, a result that manifests itself in the form of dissimilar forces being applied to the torsional wave packets. This is critically important because it can potentially lead to dissimilar torsional dynamics, which is the second criteria that must be met for deracemization to be possible.

IV. DESIGNING THE PULSE TRAIN

Based on the present information, it would be reasonable to assume that driving the oriented system with a train of pulses with a polarization axis that is de-aligned from the initial structural symmetry axis along the $\hat{x}$ coordinate will allow us increase the amplitude of the dihedral oscillations while simultaneously breaking the inversion symmetry of the enantiomeric dynamics in ϕ_d. However, there is a problem with this idea; the rotation

of both enantiomers in Φ will eventually cause $\hat{\theta}_{\text{sym}}$ to align (or nearly align) with the polarization axis of the pulse train, which will once again make it difficult to apply the dissimilar forces to the torsional motion that are required to further break the inversion symmetry of the structural dynamics.

In ref. 14 it was discovered that this problem can be addressed by driving the system with two different fields $\mathbf{E}_1$ and $\mathbf{E}_2$, where the polarization axis of $\mathbf{E}_1$ ($\mathbf{E}_2$) is rotated away from the minor alignment pulse axis ($\hat{x}$) by $-6.5°$ ($6.5°$) in the $\hat{x}\hat{y}$ plane (see, e.g., chart 2 from the same paper). This allowed the optimization algorithm to generate a combined field that changes its polarization axis over time, effectively maintaining large differences between the structural symmetry axis of the molecules and the polarization axis of the driving field. In this way, the amplitude of the torsional oscillations could be increased while maintaining the asymmetrical interaction forces that are required for the wave packet trajectories in ϕ_d to become sufficiently dissimilar over time to facilitate deracemization.

Our approach here is to once again apply the aforementioned principles by driving the system with two different fields with polarization axes that are rotated away from the lab frame $\hat{x}$ axis by equal and opposite angles in the $\hat{x}\hat{y}$ plane. However, instead of optimizing the pulse shapes, we now take a more rudimentary approach by combining the fields to make a simple train of equally spaced pulses with alternating polarization axes. Sketches illustrating this general idea are shown in figures 4 and 5. Panel 1 in figure 4 shows how the aligned system is initially driven by a pulse with a polarization axis that is rotated away from the structural symmetry axis by a positive angle. Referring back to panels (3a) and (3b) in figure 3, it can be seen that this will induce (asymmetric) torsional vibrations in the enantiomers, as well as causing both enantiomers to rotate around the lab frame $\hat{z}$ axis towards the angle of the current field polarization axis. Panel 2 of figure 4 shows how this rotation will cause the structural symmetry axis of the molecules to become aligned with the current polarization axis of the driving field, effectively leaving the system in a configuration similar to the one shown in panels (1a) and (1b) of figure 3, i.e. the forces applied to the enantiomeric wave packets in the ϕ_d coordinate will now be nearly symmetrical. To remedy this, we change the polarization axis of the next pulse in the train to the opposite angle as shown in panel 3 of figure 4. This restores the asymmetrical nature of the enantiomer/field interaction, as well as causing both enantiomers to rotate in the opposite direction around $\hat{z}$ as they move to align with the new polarization axis. When this alignment eventually

occurs, as shown in panel 4 of figure 4, the polarization direction of the driving field is changed again, and the process is repeated.

Based on this operating principle, we constructed a train of 7 Gaussian pulses where the polarization axes of the first, fourth and fifth pulses where rotated away from the $\hat{x}$ axis by 8.5°, and the axes of the second, third, sixth, and seventh pulses where rotated away from $\hat{x}$ by $-8.5°$ (see the sketch in figure 5). As the forthcoming simulated results (figure 6) will show, our strategy for choosing the polarization axis of each pulse in the combined pulse train was to simply alternate the polarization angle of the subsequent pulse any time the angle of the structural symmetry axis $\hat{\theta}_{\text{sym}}$ crosses the angle of the current pulse polarization axis. As a side note to experimentalists, figure 5 also illustrates how the suggested field polarization geometry can be achieved in a laboratory by propagating the two driving pulses along axes that are rotated away from the alignment pulse propagation ($\hat{y}$) axis by $\pm 8.5°$. While there are other directions the driving laser pulses could be applied from to achieve the same results (see, e.g., the abstract figure in ref. 14), this particular setup is advantageous because it will maximize the volume of the effective region where all three lasers overlap and interact with the molecules, which should lead to better measurement statistics.

Besides being polarized at different angles, all 7 pulses shown in figure 5 have peak intensities of 10 TW/cm^2, FWHM widths of 0.67 ps, and are equally spaced at 1.26 ps intervals. In general, the pulse parameters were chosen based on prior knowledge the system. The peak intensity was selected to approximate the intensity of the optimized pulses in ref. 14, and is expected to be well below the ionization limit[26] of the molecules. The choice of pulse spacing was based on the estimated wave packet oscillation period of $T = 1.2$ ps found in ref. 17, and the FWHM pulse widths were also defined in relation to the oscillation period based on an analysis performed in ref. 23, where it is estimated that optimal vibrational excitation with a fixed intensity Gaussian pulse is achieved when the relationship between the FWHM width and the oscillation period T is given by $\text{FWHM}/T = 2\sqrt{\ln 2}/\pi$. Note that through trial and error we found that slightly increasing the pulse spacing from 1.2 ps to 1.26 ps (while also appropriately increasing the pulse widths) yielded marginally better results in terms of induced wave packet asymmetries. Finally, while using an angle of 17° between the polarization axes of the two pulse trains gave the best results in our simulations, dealignment angles between 13° and 20° were also able to generate significant wave packet asymmetries. The message to experimentalists here is that although we have tuned our

FIG. 6. The three columns show the rotational dynamics (middle row) and dihedral dynamics (bottom row) when three different types pulse trains are applied to the 3D oriented racemic mixture of R_a (red curves) and S_a (blue curves) molecules. The pulse train in the first column corresponds to the one shown in figure 5, i.e. the polarization axes are alternated in a way that ensures that the interaction between the field and the molecules remains asymmetrical. The pulse train in the middle column corresponds to applying 7 pulses with polarization axes that are all de-aligned from the initial molecular symmetry axis by 8.5°, and the pulse train in the right hand column corresponds to applying 7 pulses with polarization axes that are all aligned with the initial molecular symmetry axis $\hat{x}$. Note that the evolution of the $\langle\phi_d\rangle$ value for the R_a enantiomer in the bottom row of plots has been multiplied by -1 to better facilitate comparison (see article text).

pulse parameters to a certain extent, we expect that there is a relatively large range of pulse parameters that will yield good results.

V. RESULTS AND DISCUSSION

The pulse trains were simulated interacting with the 3D oriented racemic mixture using split-operator propagation[27] to solve the time-dependent Schrödinger equation. The simulation results are shown in panels (1a), (1b), and (1c) in figure 6. Panel (1a) shows the intensity profiles of the pulses, panel (1b) shows the expectation value of the weighted rotational angle $\langle\Phi\rangle$ of each enantiomer, and the angle of the structural symmetry axis $\hat{\theta}_{\text{sym}}$, as a function of time. For reference, the polarization angle of the current pulse is also shown, since this is the angle that $\hat{\theta}_{\text{sym}}$ will generally rotate towards to as the dynamics evolve in time. Panel (1c) shows the corresponding evolution of the expectation value of the dihedral angle $\langle\phi_d\rangle$ of each enantiomer. Note that in panel (1c) the curve corresponding to the ϕ_d trajectory of the R_a enantiomer has been multiplied by -1 to facilitate comparison between the dynamics; i.e. when the enantiomeric dynamics in $\langle\phi_d\rangle$ are mirrored, the curves on the bottom panel will lie exactly on top of each other, and conversely, any asymmetries in the torsional dynamics will be characterized by divergence between the two curves.

Panel (1b) of figure 6 shows how alternating the polarization axis of the field as the system interacts with the pulse train shown in panel (1a) causes the rotational angles (and

This manuscript was accepted by J. Chem. Phys. Click here to see the version of record.

symmetry axis angle) of the enantiomers to oscillate back and forth around $\Phi = 0$ with steadily increasing amplitudes. This happens because the time scale of the alternations of the field polarization axis are similar to the time scale of the pendular oscillations of the molecules in the potential wells generated by the same fields. These "driven" oscillations in Φ lead to increasing dealignment angles between the structural symmetry axis of the enantiomers and the polarization axis of the driving field. As discussed (and shown in figure 3), this leads to larger asymmetries in the forces driving the torsional oscillations. The impact of these asymmetrical forces on the dihedral trajectories in $\langle\phi_d\rangle$ can clearly be seen in panel (1c), where the expected positions of the R_a and S_a wave packets in ϕ_d begin to significantly diverge at around 7 ps; in fact some degree of deracemization ends up occuring since the mean position of the R_a wave packet eventually moves over the potential barrier located at $\phi_d = 0$, while the S_a wave packet remains fairly well localized on the same side of the barrier that it started out on.

For comparison, we also drove the racemic mixture with a train of 7 pulses using the same parameters as before, except this time the polarization axes of all the pulses were dealigned from $\hat{x}$ by 8.5° (i.e. we did not alternate the polarization axes of the pulses in the driving field to ensure the asymmetrical nature of the interaction was maintained/increased). The $\langle\Phi\rangle$ and $\langle\phi_d\rangle$ dynamics generated by this pulse train are respectively shown in panels (2b) and (2c) of figure 6. In panel (2b) it can be seen that now the structural symmetry axis of the enantiomers spends most of its time aligned, or nearly aligned (within about 8°) of the polarization axis of the driving field. While the small amount of dealignment between the polarization axis and $\hat{\theta}_{\text{sym}}$ leads to minor asymmetries in the forces applied to the dihedral oscillations, it is far less than when we used the pulse train with alternating polarization axes to drive the enantiomers. This is also apparent in panel (2c), where only minor divergences between the blue and red curves are observed, i.e. the inversion symmetry in the torsional dynamics of the enantiomers becomes broken, but not to a significant degree.

As a final test, we once again drove the enantiomers using a train of pulses with the same parameters as before, except this time the polarization axes of all the pulses were aligned with $\hat{x}$. The rotational and torsional dynamics generated by this pulse train are respectively shown in panels (3b) and (3c) of figure 6, and it is apparent that they are perfectly symmetrical at all times. This is because, as stated, the field/molecule interaction in this case will always apply symmetrical forces to both enantiomeric wave packets, since

FIG. 7. Marginal probability distribution of the S_a and R_a enantiomeric wave packets projected onto the ϕ_d axis. Quantitative analysis reveals that the R_a/S_a enantiomeric fraction has now become 26/74, i.e. some deracemization has taken place. The horizontal dashed line shows the point where the difference in $\langle\phi_d\rangle$ between the R_a and S_a enantiomer is the largest, i.e. the point where the structures of the each enantiomer have, in a sense, become the most dissimilar. A sketch of how this configuration will look on the experimental detector plate is shown in figure 8.

the polarization axis of the driving field always remains parallel to the structural symmetry axis of the system. Note that the R_a and S_a dynamics in Φ are also symmetrical for this reason, although they appear to exchange positions at around 7 ps. This can be explained by considering the fact that the mean positions of both enantiomeric wave packets in ϕ_d transfer into their respective opposite wells at around 7 ps, i.e. each enantiomer has effectively been transformed into its own mirror image.

In order to better illustrate the critical elements of the evolution in the torsional states in panel (1c) from figure 6, the wave packets dynamics in the interval between 6 and 10 ps were projected onto the ϕ_d coordinate axis, resulting in the marginal probability distributions of the dihedral wave packet shown in figure 7. Here we see that the R_a wave packet becomes bifurcated on the potential barrier at $\phi_d = 0$ at around 7.5 ps, i.e. part of it is transferred into the right hand well and part of it remains in its original position in the left well. This is a similar, albeit more crude, example of what happens to the enantiomeric wave packets when the system interacts with the optimized pulse in ref. 14, where the R_a wave packet was propelled over the potential barrier separating the enantiomeric forms and the slightly dissimilar trajectory of the S_a wave packet caused it to rebound entirely back into its own well instead, leading to a deracemized mixture where 98% of the molecules were S_a enantiomers. In the present case, the simplified pulse train leads to a final S_a population of 74%. While this is certainly a result that can be improved on, achieving this in a laboratory would still be a significant and important accomplishment.

FIG. 8. Projecting $P_{\mathrm{Br}}^{\mathrm{det}}(\phi)$ and $P_{\mathrm{F}}^{\mathrm{det}}(\phi)$ onto radial surface plots illustrates the respective ion signal intensities of the ejected (a) Br and (b) F molecular fragments as they are expected to appear on the detection plates at $t = 9.1$ ps when the pulse train in figure 6(1a) is applied in an experimental situation. For comparison, the ion distributions at $t = 0$ are included as well. The details pertaining to the construction of these pictures can be found in the main article text, however the important feature to take note of is the highly asymmetrical nature of the distribution of F fragments across the vertical 0°/180° axis (dashed white line) at $t = 9.1$ ps in panel (b), as this demonstrates that the enantiomeric structures/wave packets have become very different from each other.

A. Simulating the Experimental Data

As stated at the article outset, one of the primary goals of this paper has been to suggest a relatively simple experiment that will bring experimentalists a step closer to achieving laser induced deracemization in a laboratory. For this reason, it is relevant to discuss what the measurement data generated by the pulse train in panel (1a) of figure 6 can be expected to look like.

In previous experiments, Coulomb explosion imaging has been used to determine the angular configurations of the Br- and F-substituted phenyl rings in $F_2H_3C_6 - C_6H_3Br_2$ and similar molecules[17–19,28]. This technique is based around the application of a very brief and intense probe pulse to ionize the molecules at an instant in time. The fragmented Br^+ and F^+ ions are ejected axially from the phenyl rings and accelerated along the lab-frame $\hat{z}$ axis by a static electric field until they collide with a circular detection plate oriented in the $\hat{x}\hat{y}$ plane at one end of the experimental chamber (see, e.g. figure 1 in ref. 28). Because the Br^+ and F^+ ions have different weights, they will experience different accelerations in the static field, and subsequently they will arrive at the detection plate at different times. This makes it possible to differentiate between a Br^+ and a F^+ ion hit on the detector by keeping track of the delay between the arrival of the probe pulse and the detection event. By performing repeated measurements and recording the angular distributions of the ejected Br^+ and F^+ fragments, experimentalists can construct a picture of the wave packet probability distributions corresponding to the angular configurations of the Br- and

This manuscript was accepted by J. Chem. Phys. Click here to see the version of record.

Br substituted phenyl rings at various instances in time (see, e.g. figure 3 in ref. 28).

We will now describe how we calculated simulated angular distributions of the ejected Br and F fragments as they are expected to appear on the detector plate. Let $\Psi_{R_a}(\phi_{\mathrm{Br}}, \phi_{\mathrm{F}})$ and $\Psi_{S_a}(\phi_{\mathrm{Br}}, \phi_{\mathrm{F}})$ represent the simulated 2D wave packets of the respective R_a and S_a enantiomers, now represented in the $(\phi_{\mathrm{Br}}, \phi_{\mathrm{F}})$ coordinate system. Each enantiomeric wave packet can be used to create two 1D marginal probability distributions by integrating out either ϕ_{Br} or ϕ_{F}, i.e.

$$P_{S_a}(\phi_{\mathrm{Br}}) = \int |\Psi_{S_a}(\phi_{\mathrm{Br}}, \phi_{\mathrm{F}})|^2 d\phi_{\mathrm{F}} \tag{2}$$

$$P_{S_a}(\phi_{\mathrm{F}}) = \int |\Psi_{S_a}(\phi_{\mathrm{Br}}, \phi_{\mathrm{F}})|^2 d\phi_{\mathrm{Br}} \tag{3}$$

$$P_{R_a}(\phi_{\mathrm{Br}}) = \int |\Psi_{R_a}(\phi_{\mathrm{Br}}, \phi_{\mathrm{F}})|^2 d\phi_{\mathrm{F}} \tag{4}$$

$$P_{R_a}(\phi_{\mathrm{F}}) = \int |\Psi_{R_a}(\phi_{\mathrm{Br}}, \phi_{\mathrm{F}})|^2 d\phi_{\mathrm{Br}}, \tag{5}$$

$P_{S_a}(\phi_{\mathrm{Br}})$ and $P_{S_a}(\phi_{\mathrm{F}})$ represent the angular probability distributions of the respective Br- and F-substituted ring for the S_a enantiomer, and $P_{R_a}(\phi_{\mathrm{Br}})$ and $P_{R_a}(\phi_{\mathrm{F}})$ represent the angular probability distributions of the respective Br- and F-substituted rings for the R_a enantiomer.

At this point it is important to note that in an experiment it isn't necessarily possible to tell which enantiomer a detected F^+ or Br^+ ion fragment has originated from. For this reason, $P_{S_a}(\phi_{\mathrm{Br}})$ and $P_{R_a}(\phi_{\mathrm{Br}})$ were incoherently summed to generate a distribution representing the total ion fragment signal intensity of the Br^+ ion fragments as a function of the detector plate angle:

$$P_{\mathrm{tot}}(\phi_{\mathrm{Br}}) = \frac{1}{2}[P_{S_a}(\phi_{\mathrm{Br}}) + P_{R_a}(\phi_{\mathrm{Br}})], \tag{6}$$

and $P_{S_a}(\phi_{\mathrm{F}})$ and $P_{R_a}(\phi_{\mathrm{F}})$ where combined in the same way to generate the corresponding distribution of F^+ fragments:

$$P_{\mathrm{tot}}(\phi_{\mathrm{F}}) = \frac{1}{2}[P_{S_a}(\phi_{\mathrm{F}}) + P_{R_a}(\phi_{\mathrm{F}})], \tag{7}$$

Note also that the symmetry of the phenyl rings means that whenever an ion is detected at ϕ° on the detector, another ion will appear at $(\phi + 180)^\circ$. This means that to get the angular distribution of ions as they will appear on the detector plate, the distributions $P_{\mathrm{tot}}(\phi_{\mathrm{Br}})$ and

This manuscript was accepted by J. Chem. Phys. Click here to see the version of record.

$P_{\mathrm{F}}^{\mathrm{tot}}(\phi_{\mathrm{F}})$ have to be added to versions of themselves where the locations of the distributions have been shifted forward by 180°:

$$P_{\mathrm{Br}}^{\mathrm{det}}(\phi) = \frac{1}{2}\left[P^{\mathrm{tot}}(\phi_{\mathrm{Br}}) + P^{\mathrm{tot}}(\phi_{\mathrm{Br}} + 180)\right] \tag{8}$$

$$P_{\mathrm{F}}^{\mathrm{det}}(\phi) = \frac{1}{2}\left[P^{\mathrm{tot}}(\phi_{\mathrm{F}}) + P^{\mathrm{tot}}(\phi_{\mathrm{F}} + 180)\right], \tag{9}$$

where we introduce ϕ as a general coordinate representing the angle in the $\hat{x}\hat{y}$ plane with relation to the lab-frame $\hat{x}$ axis (i.e. the detector plate angle). $P_{\mathrm{Br}}^{\mathrm{det}}(\phi)$ and $P_{\mathrm{F}}^{\mathrm{det}}(\phi)$ were then projected onto radial surface plots in order to replicate the form of, e.g., the raw experimental data displayed in figure 3 in ref. 28. A plot of this result is shown in figure 8, where we have chosen to illustrate what the angular distributions of the ejected Br and F ions will look like on the detector plate at the moment in time when the difference between the expectation value of the R_a dihedral angle $\langle\phi_d\rangle_{\mathrm{R_a}}$ and the S_a dihedral angle $\langle\phi_d\rangle_{\mathrm{S_a}}$ is largest, which we determined would occur at about 9.1 ps (as indicated by the black dashed horizontal lines in figure 7).

Note that we are only interested in the internal structure of the molecules, since their orientations in Φ do not directly relate to, or characterize, the process of deracemization. For this reason, the effect of external rotations of the molecules as they appear on the detector plate plots in figure 8 have been corrected (i.e. eliminated) by rotating the plotted distributions towards the 0° axis of the radial surface plots by an angle equivalent to the mean angular position of the Br rings. Effectively, this leads to a picture where the mean position of each Br ring will be mirrored across the vertical 0°/180° axis, as shown in figure 8(a). This makes it easier to see the asymmetries present in the internal structures of the enantiomers (i.e. ϕ_d), as they will be clearly visible as asymmetries across the 0°/180° axis in the distribution of F fragments shown in figure 8(b).

For comparison, the simulated Br^+ and F^+ ion fragment distributions at $t = 0$ are also included in the bottom left corner of panels (a) and (b) in figure 8, respectively. These initial distributions show the characteristic symmetrical "four-dot" geometry that has been experimentally observed before (see, e.g., figure 1 in ref. 28). Conversely, the illustration at $t = 9.1$ in figure 8(b) indicates that the angular distribution of the F^+ fragments has become highly asymmetrical, and the effect should be easy to see in a laboratory setting despite the presence of confounding factors such as experimental noise. While the qualitative analyses of the general system dynamics and its response to a field discussed throughout this paper

This manuscript was accepted by J. Chem. Phys. Click here to see the version of record.

have been inspired by a classical picture (i.e. the molecular configurations in Φ and/or ϕ_d have generally not been described as probability distributions), figures 7 and 8 show that applying asymmetrical forces to the enantiomeric wave packets can also have a significant impact on the wave packet shapes and not just their expected positions. This is useful because it makes it even easier to see the asymmetries in an experimental situation, e.g. in figure 8(b) there is a strong peak in the distribution at about $130°/-50°$ that is caused by the relatively well-localized dihedral wave packet of the S_a enantiomer (see figure 7(a)), whereas the spread out areas of the distribution with lower signal intensity are cause by the bifurcation and subsequent delocalization of the R_a dihedral wave packet (see figure 7(b)).

B. Robustness Check

Since we are using a simplified 2D model of a real system that has many more degrees of freedom, it is important to investigate how errors or discrepancies in the calculated potential energy surface (in particular, the characteristics of the energy barrier separating the enantiomers) may affect the simulated dynamics. To investigate this, we ran two new simulations using identical pulse parameters, where the height of the saddle point around $(\phi_d = 0, \Phi = 0)$ had been artificially increased/decreased by $\pm 30\%$. We found that this did not significantly change the qualitative features of the results. We also investigated what happens when we change the applied pulse intensities by $\pm 10\%$ (in a rough sense, this is equivalent to checking how inaccuracies in the calculated polarizability function might affect the dynamics). We found that this did not significantly change the nature of the resulting dynamics either. If we decreased the pulse intensities by more than $\sim 10\%$, we found that both enantiomeric wave packets remained localized in their original wells. In such a case, the resulting asymmetries in the system may be harder to detect. The message here is that if this situation is encountered when attempting the actual experiment, the issue may be remedied by appropriately increasing the peak intensity of the pulse trains (if increasing the intensity is not possible, an alternative solution may be to extend the pulse train by including additional pulses).

As outlined in Ref. 17, the second lowest frequency normal mode has a Raman cross section that is not negligible compared to the cross section of the lowest frequency (torsional) mode, and as such this mode may also become activated when the molecule interacts with

ing laser pulse. However, this mode does not contain any torsional motion, and its activation is therefore not expected to *directly* impact the dynamics of the torsional wave packet other than possibly modifying the potential energy surface. As outlined in the previous paragraph, we predict our model is moderately robust to this kind of discrepancy. This does, however, allude to a more complicated issue related to the fact that normal modes are only uncoupled when the amplitude of the oscillations are small. As the dihedral oscillations in our simulation are large, intramolecular vibrational energy redistribution (IVR)[29] may play a significant role in the overall dynamics of the system. Whether or not IVR will be detrimental to the quality of our predicted results in an experimental situation is an open question.

As a final aside, it is important to note that molecular 3D orientation is a difficult task in practice. For example, in ref. 20 they are only able to orient the molecules so 54% of them point in the same direction (whereas ideally this number should be much closer to 100%). However, it is also shown in ref. 20 that that it is possible to differentiate between ions ejected from molecules pointing towards the detector plate and those oriented in the opposite direction due to the slight differences in flight times (leading to, e.g., the double peaks shown in figure 3 of the same article). This indicates that, in lieu of achieving a high degree of 3D orientation, it should be possible to calibrate the detection windows so they only measure ion signals from aligned molecules that are pointing in the same direction.

VI. CONCLUSION

In this paper we have suggested a relatively simple method of driving a racemic mixture of 3D oriented biphenyl $F_2H_3C_6 - C_6H_3Br_2$ molecules with a train of Gaussian pulses with alternating polarization axes. Using numerical simulations, we have shown that this will increase the amplitude of the torsional oscillations between the phenyl rings and break the symmetry of the dynamics between the left- and right-handed enantiomeric forms.

We elucidate the fundamental principles behind our approach by describing the dynamic response of the enantiomers to the applied field in a coordinate system where the kinetic energy of the external/rotational and internal/conformational dynamics are decoupled. We show that rotating the polarization axis of the driving field away from the shared structural symmetry axis of the molecules will apply asymmetrical forces to the enantiomeric wave

packets in the dihedral coordinate. This will in turn break the inversion symmetry of the dihedral dynamics, which is critical for deracemization to occur.

Finally, we show how to maximize the broken dynamic inversion symmetry by properly alternating the polarization axis of the pulses in the driving field. We use numerical simulations to demonstrate that this approach will lead to significant, and most importantly, *experimentally measurable* structural differences between the enantiomers when detected by Coulomb explosion imaging.

The strategy proposed in this paper could also be used on similar axially chiral molecules, where rotation about single bonds involve relatively small barriers. When rotation about double bonds is involved a realistic scheme for conversion would, most likely, involve excited electronic states. The same holds for more general types of chirality.

ACKNOWLEDGMENTS

The authors wish to thank Professor Henrik Stapelfeldt and his group for providing us with invaluable information and the inspiration to write this paper.

REFERENCES

[1]R. McKendry, M.-E. Theoclitou, T. Rayment, and C. Abell, Nature **391**, 566 (1998).

[2]R. Noyori, Angew. Chem. Int. Ed. **41**, 2008 (2002).

[3]A. Salam and W. Meath, Chem. Phys. **228**, 115 (1998).

[4]Y. Fujimura, L. González, K. Hoki, J. Manz, and Y. Ohtsuki, Chem. Phys. Lett. **306**, 1 (1999).

[5]Y. Fujimura, L. González, K. Hoki, D. Kröner, J. Manz, and Y. Ohtsuki, Angew. Chem. Int. Ed. **39**, 4586 (2000).

[6]M. Shapiro and E. Frishman, Phys. Rev. Lett. **84**, 1669 (2000).

[7]H. Umeda, M. Takagi, S. Yamada, S. Koseki, and Y. Fujimura, J. Am. Chem. Soc. **124**, 9265 (2001).

[8]K. Hoki, D. Kröner, and J. Manz, Chem. Phys. **267**, 59 (2001).

[9]K. Hoki, L. González, and Y. Fujimura, J. Chem. Phys. **116**, 2433 (2002).

[10]S. S. Bychkov, B. A. Grishanin, V. N. Zadkov, and H. Takahashi, J. Raman Spectrosc. **33**, 962 (2002).

[11]P. Král, I. Thanopulos, M. Shapiro, and D. Cohen, Phys. Rev. Lett. **90**, 03001 (2003).

[12]D. Gerbasi, M. Shapiro, and P. Brumer, J. Chem. Phys. **124**, 074315 (2006).

[13]S. M. Parker, M. A. Ratner, and T. Seideman, Mol. Phys. **110**, 1941 (2012).

[14]E. F. Thomas and N. E. Henriksen, J. Phys. Chem. Lett. **8**, 2212 (2017).

[15]M. Mitchell, *An Introduction to Genetic Algorithms*, 5th ed. (The MIT Press, 1999).

[16]A. Monmayrant, S. Weber, and B. Chatel, J. Phys. B **43**, 103001 (2010).

[17]C. B. Madsen, L. B. Madsen, S. S. Viftrup, M. P. Johansson, T. B. Poulsen, L. Holmegaard, V. Kumarappan, K. A. Jørgensen, and H. Stapelfeldt, J. Chem. Phys. **130**, 234310 (2009).

[18]C. B. Madsen, L. B. Madsen, S. S. Viftrup, M. P. Johansson, T. B. Poulsen, L. Holmegaard, V. Kumarappan, K. A. Jørgensen, and H. Stapelfeldt, Phys. Rev. Lett. **102**, 073007 (2009).

[19]L. Christensen, J. H. Nielsen, C. B. Brandt, C. B. Madsen, L. B. Madsen, C. S. Slater, A. Lauer, M. Brouard, M. P. Johansson, B. Shepperson, and H. Stapelfeldt, Phys. Rev. Lett. **113**, 073005 (2014).

[20]H. Tanji, S. Minemoto, and H. Sakai, Phys. Rev. A **72**, 063401 (2005).

[21]D. Townsend, B. J. Sussman, and A. Stolow, J. Phys. Chem. A **115**, 357 (2011).

[22]B. J. Sussman, Am. J. Phys **79**, 477 (2011).

[23]E. F. Thomas and N. E. Henriksen, J. Chem. Phys. **144**, 244307 (2016).

[24]R. Kosloff and H. Tal-Ezer, Chem. Phys. Lett. **127**, 223 (1986).

[25]A. M. Wiener, D. E. Leaird, G. P. Wiederrecht, and K. A. Nelson, J. Opt. Soc. Am. B **8**, 1264 (1991).

[26]S. M. Hankin, D. M. Villeneuve, P. B. Corkum, and D. M. Rayner, Phys. Rev. Lett. **84**, 5082 (2000).

[27]R. Kosloff, J. Phys. Chem. **92**, 2087 (1988).

[28]J. L. Hansen, J. H. Nielsen, C. B. Madsen, A. T. Lindhardt, M. P. Johansson, T. Skrydstrup, L. B. Madsen, and H. Stapelfeldt, J. Chem. Phys. **136**, 204310 (2012).

[29]D. J. Nesbitt and R. W. Field, J. Phys. Chem. **100**, 12735 (1996).

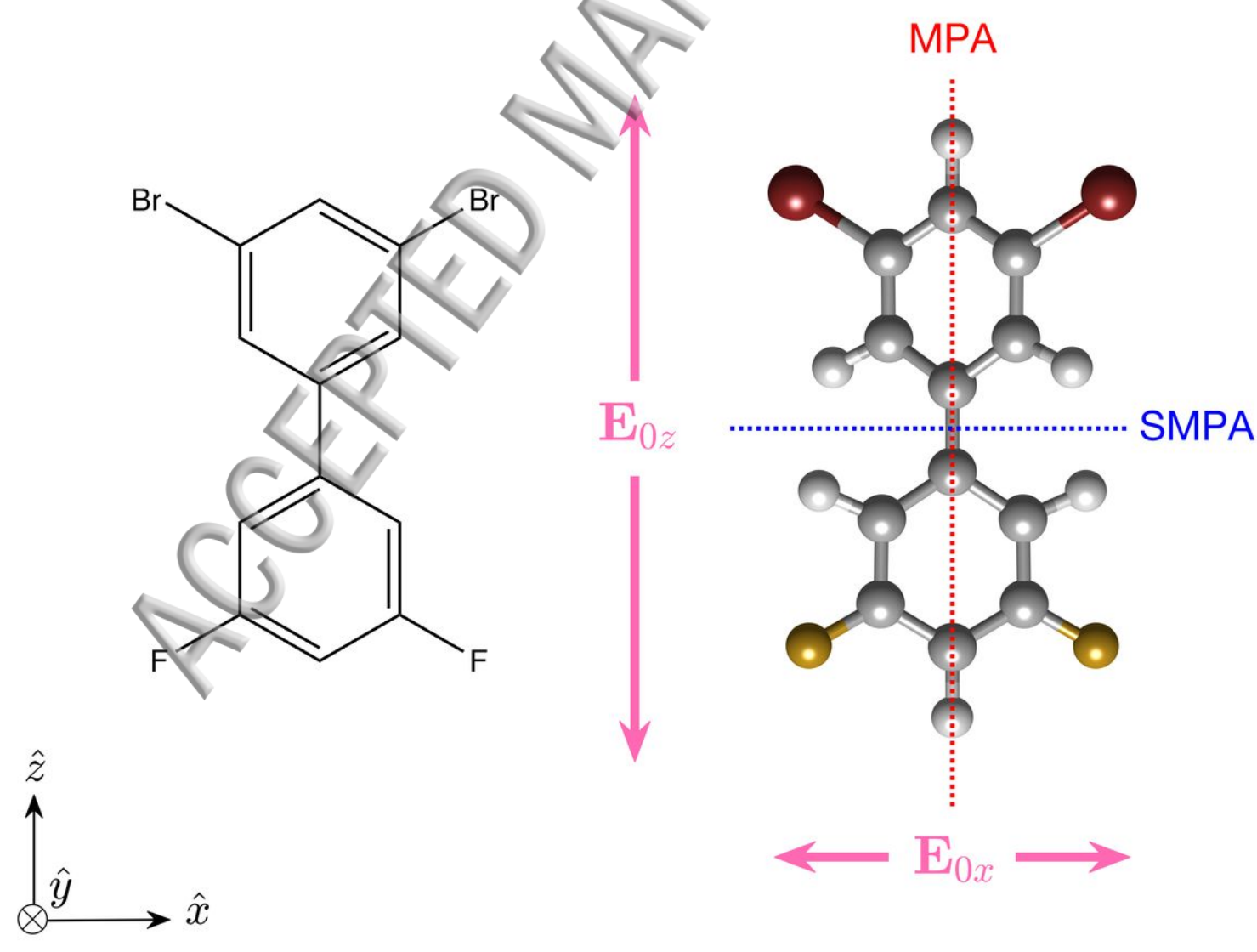

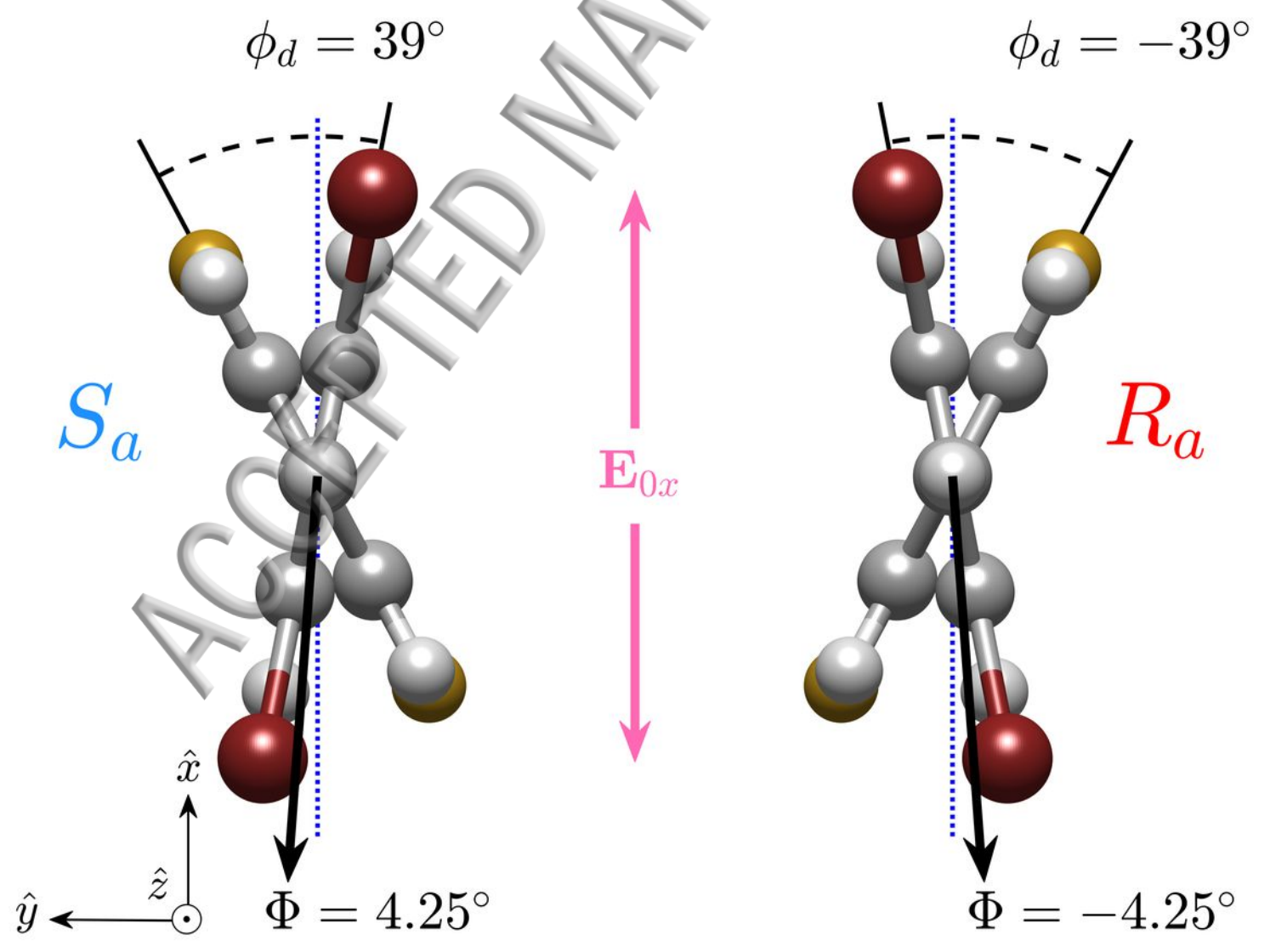

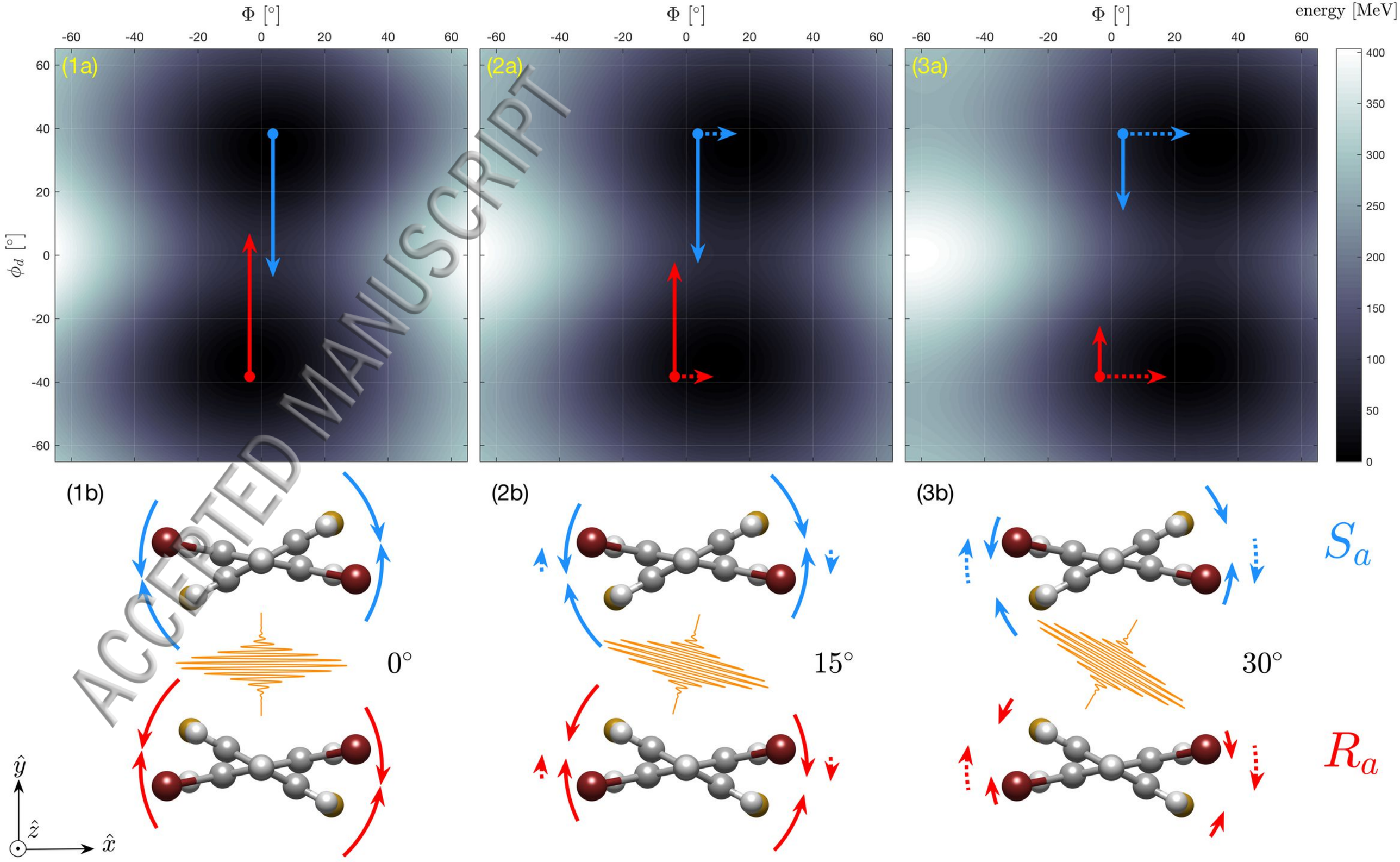

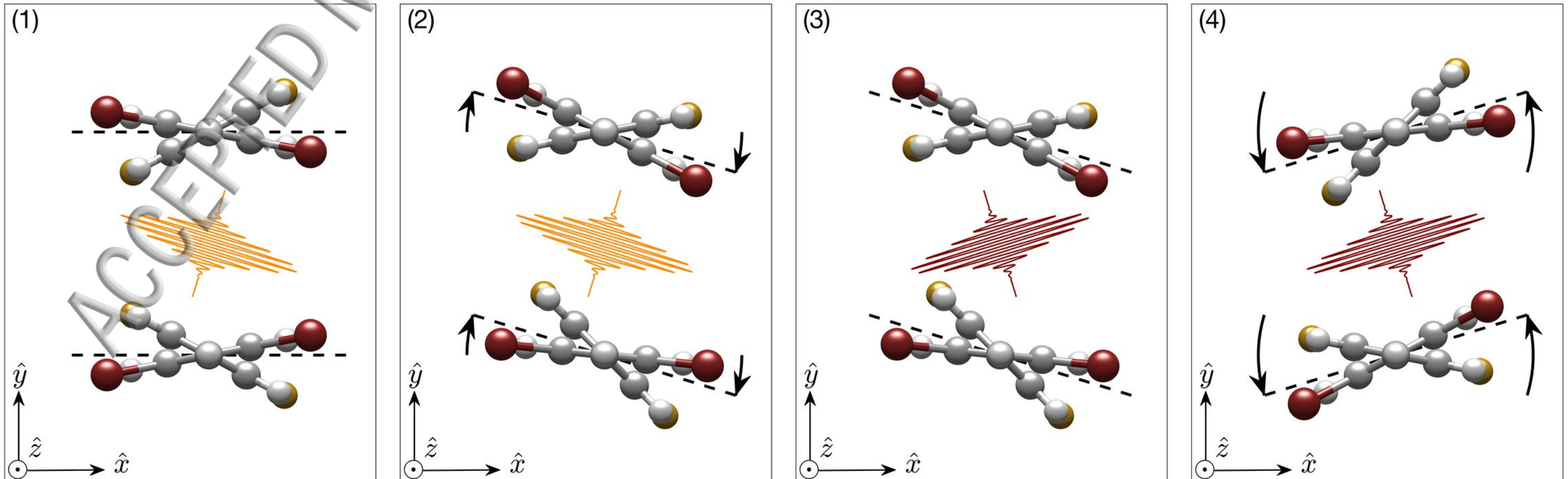

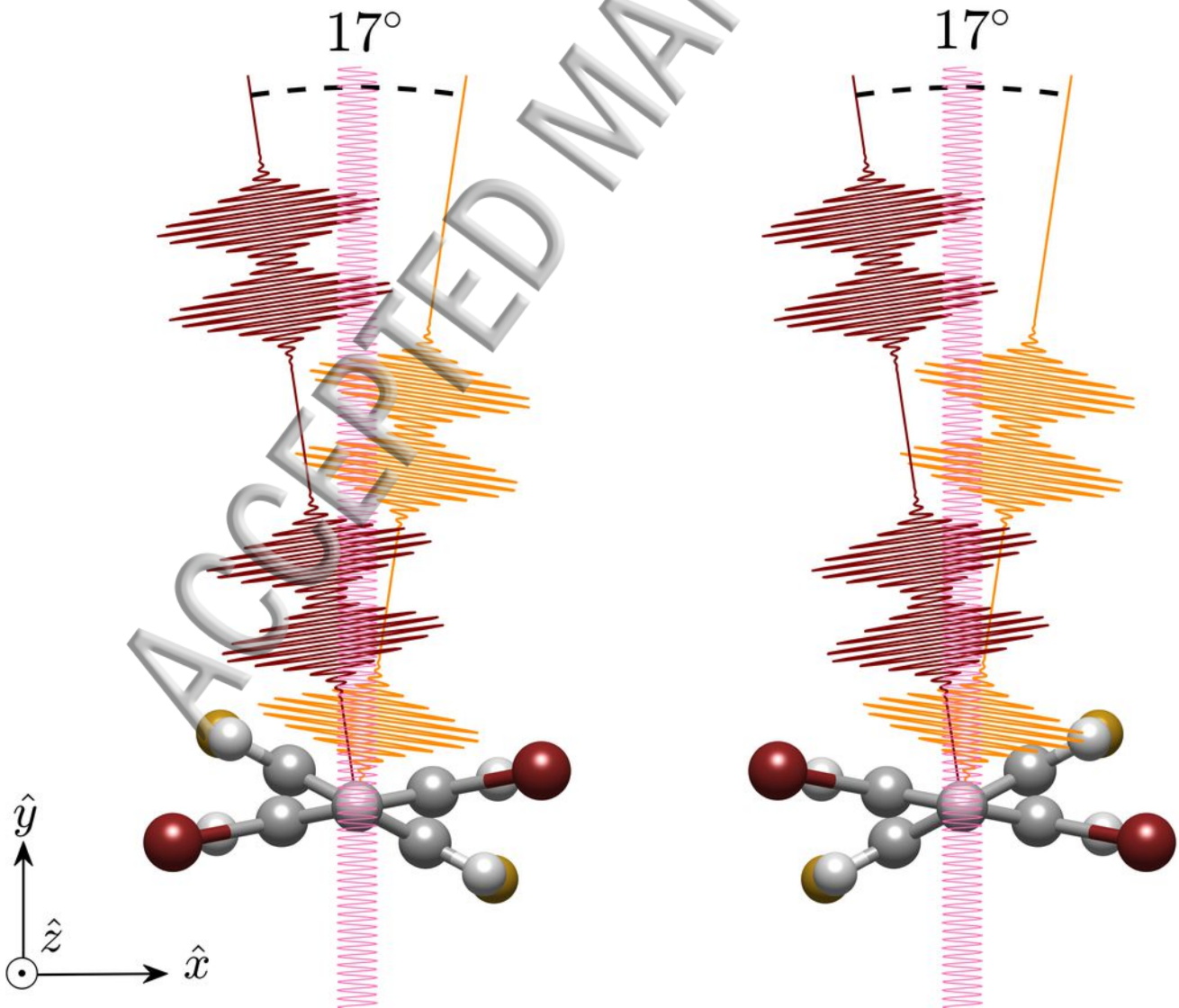

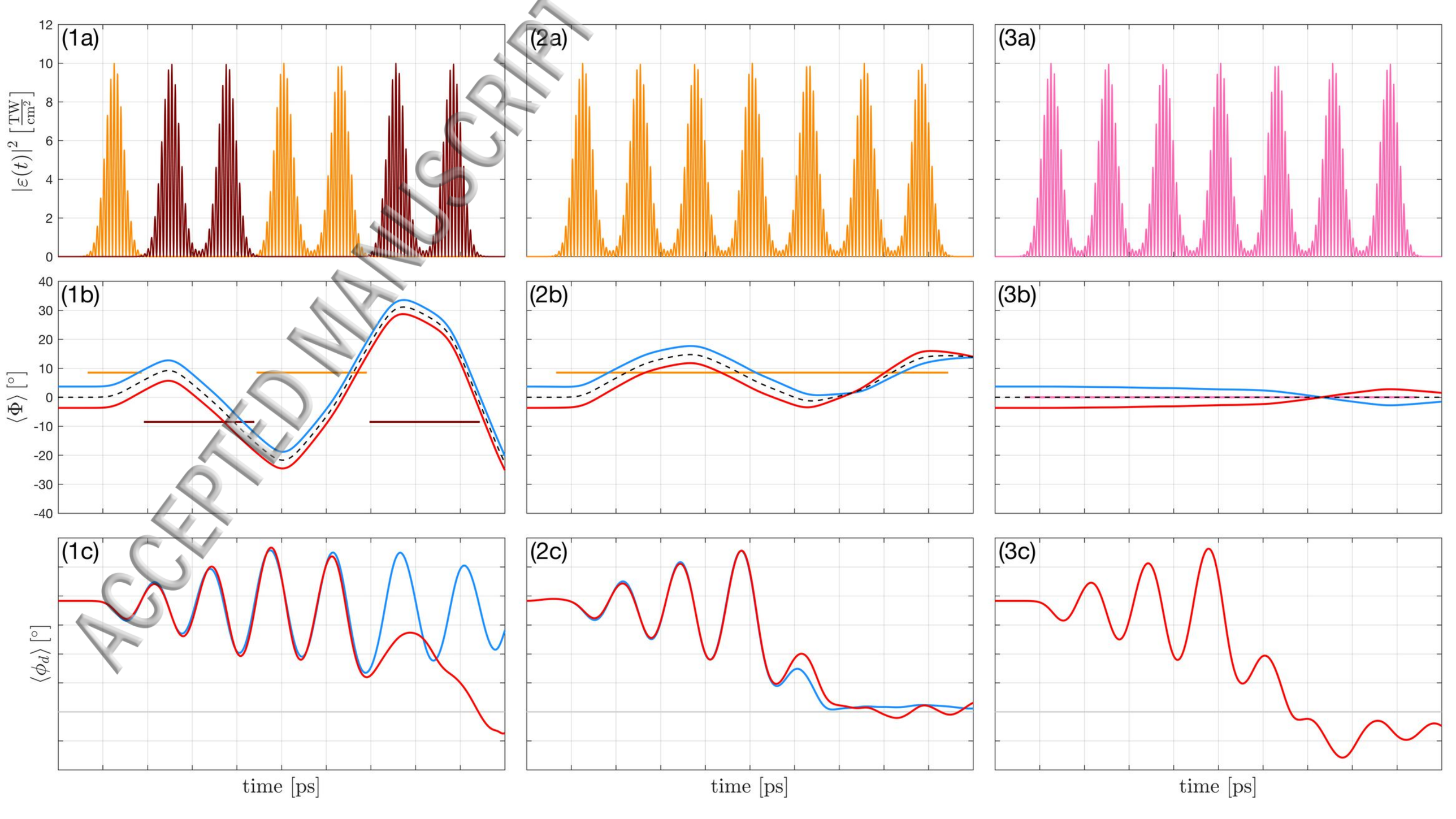

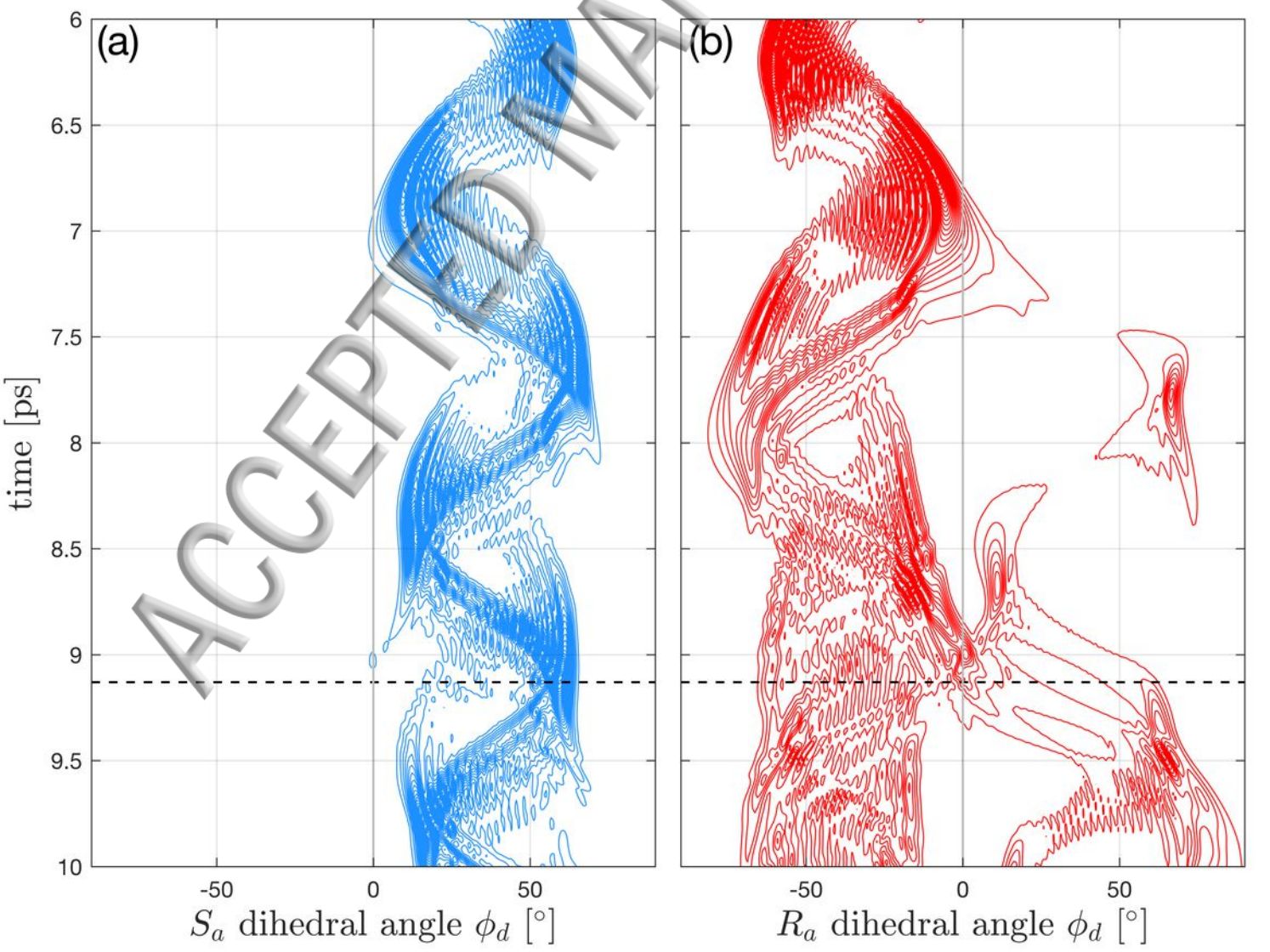
(a)
(b)
time [ps]
6
6.5
7
7.5
8
8.5
9
9.5
10
-50
0
50
S_a dihedral angle ϕ_d [°]
-50
0
50
R_a dihedral angle ϕ_d [°]